Check for updates

Comprehensive studies to improve ultrasensitive detection of HIV-1 p24 antigen†

Evan Reboli,[a] Ajoke Williams,[a] Ankan Biswas,[a] Tianwei Jia,[b] Ying Luo,[c] Mukesh Kumar[d] and Suri Iyer [iD] *[a]

Early and accurate detection of HIV-1 p24 antigen is crucial for timely diagnosis and treatment, particularly in resource-limited settings where traditional methods often lack the necessary sensitivity for early-stage detection or is expensive. Here, we developed a layer-by-layer signal amplification platform employing fluorescent silica nanoparticles functionalized *via* bioorthogonal TCO/TZ chemistry. We evaluated nanoparticles of different sizes (25, 50, and 100 nm) and two dye-doped nanoparticle formulations to optimize signal intensity, detection limits, and nonspecific binding. The 25 nm RITC-doped nanoparticles demonstrated superior performance, achieving an ultra-low detection limit of 7 fg mL^{-1} with a broad linear range up to 1 ng mL^{-1}. Compared to FITC-doped nanoparticles, RITC-doped nanoparticles provided enhanced brightness and signal strength. Further optimization revealed that using 50 μg of 25 nm nanoparticles yielded the best sensitivity while minimizing nonspecific binding. This nanoparticle-based assay significantly outperformed commercial ELISA kits, offering a broad dynamic range and improved sensitivity. Our platform presents a highly sensitive and adaptable approach for HIV-1 p24 antigen detection, with broad potential applications in point-of-care diagnostics and detection of other low-abundance biomarkers, ultimately enhancing early disease detection and treatment accessibility.

Introduction

Human immunodeficiency virus (HIV) remains a global health challenge, with 40 million people living with the virus, including 1.3 million newly infected individuals, according to United Nations Program on HIV/AIDS reports (UNAIDS 2023).[1,2] With millions of individual infected and unaware of their status, HIV testing is essential for diagnosing new infections and for monitoring the viral loads.[3] Therefore, it is very important to develop a detection strategy for early diagnosis and clinical treatment.[4]

Detection of HIV mainly relies on HIV antibodies in the blood, but in early stages these antibodies may not be present making this method less effective.[5] Therefore nucleic acid amplification testing (NAAT) is used to detect presence of HIV RNA.[6] Although advancements in mutualization and nucleic acid amplifications have been made these tests are still cost prohibitive for resource-poor areas.[6,7] CRISPR-based methods, while highly promising, offer rapid and sensitive HIV RNA detection but require expensive instruments, trained personnel and is cost prohibitive.[8] Early detection enables the prompt start of antiretroviral therapy (ART), which is crucial for controlling the viral concentration, and preventing the progression to acquired immunodeficiency syndrome (AIDS).[9] Children born to HIV-positive mothers can contract the virus through breast milk, making regular testing essential for the early detection of infection. Early diagnosis could help prevent this by providing timely information.[10] Monitoring the viral load in children with HIV is crucial for tracking disease progression and determining when to adjust antiretroviral therapies.[11] Fingerpick blood sampling is the most used biochip in point-of-care biomarker testing due to its minimally invasive nature, making it a practical alternative for HIV detection, particularly in low-resource settings where conducting full blood tests and utilizing hematology analyzers is not feasible.[12,13]

HIV p24 antigen is a well-conserved structural protein within HIV and is used to monitor viral load.[14] p24 antigen can be detected using fourth-generation point-of-care (POC) lateral flow immunoassays approximately 15 days after HIV infection.[15,16] However, it remains a challenge early in infection and detecting

[a] *Department of Chemistry, Kennedy College of Science, University of Massachusetts Lowell, 520 Olney Science Center, Lowell, Massachusetts 01854, USA. E-mail: Sure_iyer@uml.edu*
[b] *Department of Surgery, Beth Israel Deaconess Medical Center, Harvard Medical School, National Center for Functional Glycomics, CLS 11087-3 Blackfan Circle, Boston, Massachusetts 02115, USA*
[c] *Department of Chemistry, Center for Diagnostics and Therapeutics, Georgia State University, 788 Petit Science Center, Atlanta, Georgia 30302, USA*
[d] *Department of Biology, Center for Diagnostics and Therapeutics, Georgia State University, 622 Petit Science Center, Atlanta, Georgia 30302, USA*
† Electronic supplementary information (ESI) available. See DOI: https://doi.org/10.1039/d5sd00011d

lower concentrations. Recently, we reported an ultrasensitive p24 assay with 46 fg mL^{-1} (1.84 fM) limit of detection (LOD) and a very broad linear range spanning 8 orders of magnitude, 46 fg mL^{-1} to 10 ng mL^{-1}, utilizing a layer-by-layer fluorescent silica nanoparticles and bioorthogonal chemistries.[17] The signal enhancement strategy shown in Fig. 1. First, anti-p24 antibodies are coated on the plate and blocked. Next varying concentrations of p24 are added and subsequently washed to remove unbound antigen. A secondary antibody modified with tetrazine (Ab$_2$-TZ) is added, creating a sandwich of the antigen between two antibodies. After washing to remove excess Ab$_2$-TZ, silica nanoparticles doped with either fluorescein isothiocyanate (FITC) or rhodamine B isothiocyanate (RITC) and functionalized with *trans*-cyclooctene (TCO) (FITC-SiO$_2$-PEG$_{5k}$-TCO & RITC-SiO$_2$-PEG$_{5k}$-TCO) are added to the microwell. The FITC-SiO$_2$-PEG$_{5k}$-TCO reacts with the tetrazine (TZ) conjugated to the antibody creating the first layer. Excess particles are washed leaving the first layer of bound particles, with unreacted TCO on their surfaces. The second layer is formed by the addition of the dye-doped silica nanoparticles functionalized with TZ (FITC-SiO$_2$-PEG$_{5k}$-TZ & RITC-SiO$_2$-PEG$_{5k}$-TZ), which readily reacts with unbound TCO forming the second layer with bound TZ particles. Similar to the first layer, particles functionalized with TCO can be added to further enhance the signal.

Hence, we focused our efforts on studying the effect of (1) nanoparticles of varying sizes (25 nm, 50 nm, and 100 nm) to potentially optimize their packing density around Ab$_2$-TZ and (2) increasing the "brightness" of the particles by encapsulating them with a brighter dye (RITC).

Functionalized FITC-doped nanoparticles have been extensively employed in various *in vivo* applications due to their exceptional photostability. Building on their success in other imaging techniques, we initially investigated their potential as signal enhancers in a novel layer-by-layer assay.[18,19] To further enhance signal intensity, we aimed to identify a dye with superior brightness.

The molecular brightness of a fluorophore is a critical factor in fluorescence-based applications, it is determined by the product of its molar absorptivity (ε) and fluorescence quantum yield (Φ), which collectively dictate the total light absorbed and the efficiency of fluorescence emission.[20] Consequently, we replaced FITC with rhodamine B isothiocyanate (RITC), a rhodamine derivative with a molar absorptivity of 106 000 M^{-1} cm^{-1} and a fluorescence quantum yield of 1.06, resulting in a molecular brightness of 112 360 M^{-1} cm^{-1}.[21,22] This represents an approximate 20% increase in brightness compared to fluorescein derivatives, which have a molar absorptivity of 78 000 M^{-1} cm^{-1} and a quantum yield of 0.92, yielding a molecular brightness of 71 760 M^{-1} cm^{-1}.[23,24]

In addition to enhanced brightness, rhodamine derivatives offer several advantages over fluorescein, including longer excitation and emission wavelengths, higher quantum efficiency, and improved water solubility. Furthermore, their distinct color shifts and elevated relative fluorescence units (RFU) make them particularly valuable for fluorescence-based biosensing applications.[25]
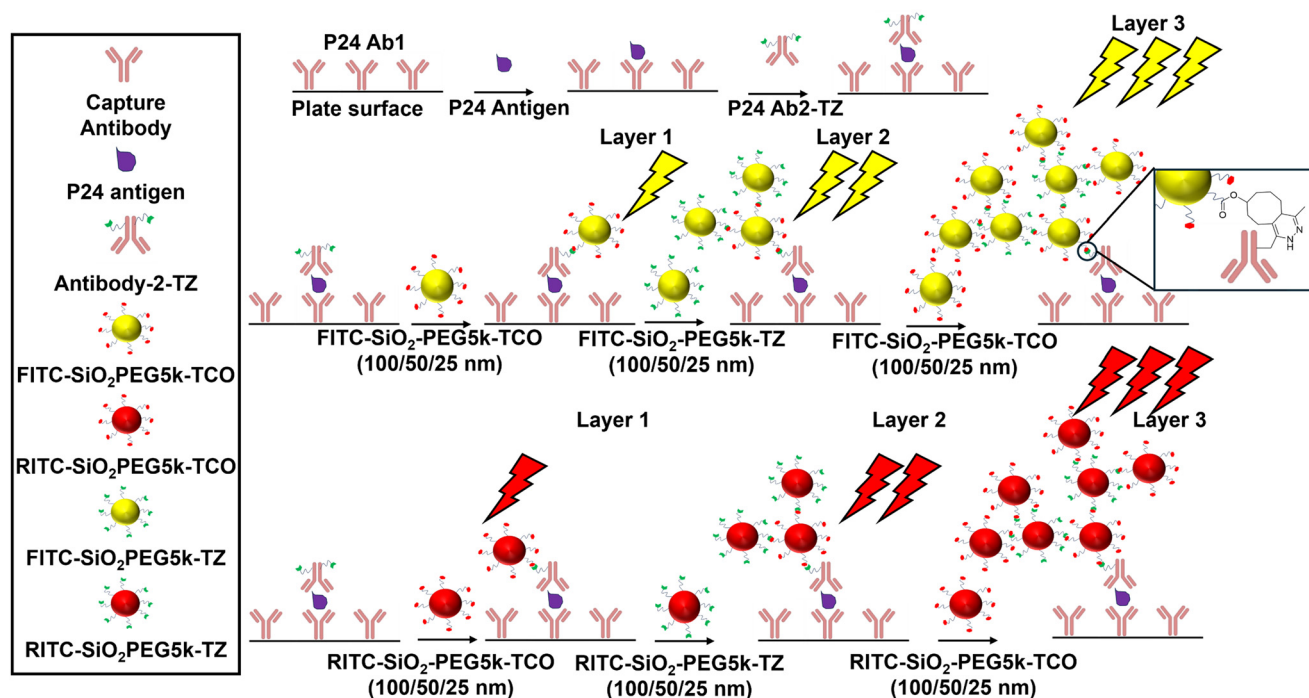

Fig. 1 Schematic of layer-by-layer signal enhancement strategy for ultrasensitive HIV-1 p24 antigen detection using fluorescent-doped nanoparticles. Shown left are assay components, top center displays FITC-SiO$_2$-PEG$_{5k}$-TZ/TCO particles, center bottom RITC-SiO$_2$-PEG$_{5k}$-TZ/TCO particles.

Experimental

Materials and equipment

Tetraethyl orthosilicate (TEOS), 3-aminopropyl triethoxysilane (APTES), fluorescein isothiocyanate (FITC, isomer I), dimethylformamide (DMF), triethylamine (TEA), ammonium hydroxide (NH_4OH), N-hydroxysuccinimide (NHS), 1-ethyl-3-(3-dimethylaminopropyl)carbodiimide (EDC), hydrochloric acid (HCl), sodium hydroxide (NaOH), phosphate-buffered saline (PBS), bovine serum albumin (BSA), sulfo-NHS, Tween 20, and ethanol were purchased from Sigma-Aldrich. PEG-bis-CH_2CO_2H, MW 5000, (COOH-5k-PEG-COOH), methyltetrazine-PEG_4-amine HCl salt (Tz-PEG_4-NH_2^*HCl), and TCO-PEG6-amine (TCO-PEG_6-NH_2) were purchased from BroadPharma. The mouse anti-HIV-1 p24 paired antibody and recombinant HIV-1 p24 protein were purchased from Prospec Protein Specialists, USA. Rhodamine B isothiocyanate (RITC), and absolute ethanol (EtOH) were purchased from Fisher Scientific. All chemicals were used as received without further purification. Ultrapure water obtained from a Millipore water purification system (18.2 MΩ cm^{-1}, Milli-Q, Merck Millipore, Darmstadt, Germany) was used in all experiments.

Zeta-potential were measured by the Horiba SZ-100 Dynamic Light Scattering (DLS) Instrument, plates were read using the molecular devices spectra Max M3 (Plate Reader), and transmission electron microscopy (TEM) images were generated *via* the Philip CM12 transmission electron microscope.

Synthesis of FITC-SiO_2-OH 100 nm and fabrication of FITC-SiO_2-NH_2, FITC-SiO_2-PEG_{5k}-COOH, FITC-SiO_2-PEG_{5k}-TZ, FITC-SiO_2-PEG_{5k}-TCO 100 nm

All reactions were performed under inert atmosphere as described in our previously reported paper.[17]

Synthesis of FITC-SiO_2-OH 50 nm nanoparticles

FITC-SiO_2-OH was prepared according to reported procedures with modifications.[26] In a 100 mL round-bottomed flask, FITC (10 mg) was mixed with EtOH (5 mL). APTES (20 µL, 0.085 mmol) was added under inert conditions. The mixture was stirred for 24 h at rt to yield the FITC–APTES adduct. Next absolute EtOH (50 mL), TEOS (0.75 mL, 3.36 mmol), NH_4OH (30%, 2.1 mL) were added. The reaction mixture was stirred for 24 h at rt. The yellow dispersion was washed with absolute EtOH (10 mL × 3) through cycles of centrifugation (10 000g, 20 min)/sonication/redispersion. Finally, the yellow nanomaterial was redispersed in absolute EtOH (10 mL). RITC-SiO_2-OH was prepared in a similar manner.

Fabrication of FITC-SiO_2-NH_2 50 nm nanoparticles. The surface modification of FITC-SiO_2-OH with APTES was performed in an EtOH solution at 90 °C. APTES (400 µL, 1.7 mmol) was added to FITC-SiO_2-OH (60 mg) in absolute EtOH (10 mL). The mixture was stirred for 24 h. FITC-SiO_2-NH_2 was separated from the mixture by centrifugation (10 000 × g, 20

min) and washed with EtOH 3×. The EtOH was removed, and the material was dried *in vacuo* for 2 h.

Fabrication of FITC-SiO_2-PEG_{5k}-COOH 50 nm nanoparticles. HOOC-PEG_{5k}-COOH (50 mg, 10 µmol) was dissolved in DMF (2 mL). EDC-HCl (2 mg, 10 µmol) and NHS (2 mg, 10 µmol) were each dissolved in DMF (400 µL) and added respectively. The mixture was stirred at rt for 30 min. FITC-SiO_2-NH_2 (30 mg) was suspended in DMF (1 mL) and added to the first solution which was stirred for 24 h. The obtained nanoparticles were separated from the mixture by centrifugation (10 000 × g, 20 min) and washed with DMF 3× and EtOH 3×. The EtOH was removed, and the material was dried *in vacuo* for 2 h.

Fabrication of FITC-SiO_2-PEG_{5k}-TZ 50 nm nanoparticles. FITC-SiO_2-PEG_{5k}-COOH (5 mg) was resuspended in DMF (1 mL). EDC-HCl (2 mg, 10 µmol) and NHS (2 mg, 10 µmol) were each dissolved in DMF (400 µL) and added, respectively. The mixture was stirred at rt for 30 min. TZ-PEG_6-NH_2 (2 mg) dissolved in DMF (200 µL) was added to the mixture and stirred for 24 h. The resulting nanoparticles were separated by centrifugation (10 000 × g, 20 min), washed with EtOH (1 mL) 3×, and PBS (1 mL) 3×. The final FITC-SiO_2-PEG_{5k}-TCO nanoparticles were resuspended in PBS (5 mg mL^{-1}). The resulting stock solution was stored at 4 °C for further experimentation.

Fabrication of RITC-SiO_2-PEG_{5k}-TCO 50 nm nanoparticles. These nanoparticles were fabricated in a manner like the fabrication of FITC-SiO_2-PEG_{5k}-TZ using TCO-PEG_6-NH_2 instead of TZ-PEG_4-NH_2.

Fabrication of RITC-SiO_2-TZ 50 nm nanoparticles. Same protocols have followed as FITC-SiO_2-TZ by using RITC (10 mg) instead of FITC (10 mg).

Synthesis of FITC-SiO_2-OH 25 nm nanoparticles

Initially FITC (10 mg) was mixed with EtOH absolute (1 mL) and APTES (140 µL, 0.6 mmol) in a round bottom flask under inert conditions. The mixture was stirred for 18 h forming a FITC–APTES adduct. To a flask containing EtOH (30 mL), TEOS (1.2 mL, 5.8 mmol), and NH_4OH (30% aq solution, 1.2 mL) FITC–APTES adduct quickly was added (100 µL). This reaction was stirred vigorously for 24 h at rt, under inert conditions. After 24 h, TEOS (240 µL, 1.2 mmol) was added to the reaction mixture at rt under inert conditions and stirred vigorously for a further 24 h. The yellow dispersion was washed with absolute ethanol 3× (10 mL) through cycles of centrifugation (15 000g, 25 min)/sonication/redispersion. Finally, the nano material was redispersed in EtOH (5 mL).

Fabrication of FITC-SiO_2-NH_2, FITC-SiO_2-PEG_{5k}-COOH, FITC-SiO_2-PEG_{5k}-TZ, FITC-SiO_2-PEG_{5k}-TCO. Fabrication of FITC-SiO_2-NH_2, FITC-SiO_2-PEG_{5k}-COOH, FITC-SiO_2-PEG_{5k}-TZ, FITC-SiO_2-PEG_{5k}-TCO were all synthesized similar manner to the 100 and 50 nm particles.

Preparation of the tetrazine-modified antibody (Ab₂-TZ). 100 µg of p24 antibody was prepared and characterized according to previously described methods.[17]

Determination of the limit and range of detection in PBS. To evaluate the sensitivity of the platform, different concentrations of p24 (0.1 fg mL^{-1}–10 ng mL^{-1}) in PBS were used. Capture antibody (3 µg), FITC-SiO$_2$-PEG$_{5k}$-TCO (50 µg), FITC-SiO$_2$-PEG$_{5k}$-TZ (50 µg), RITC-SiO$_2$-PEG$_{5k}$-TCO (50 µg), RITC-SiO$_2$-PEG$_{5k}$-TCO (50 µg), and Ab$_2$-TZ (1 µg) were used for all analyses except concentration optimization studies. LOD was determined based on the following standard calculations LOD = blank (mean) + 3× blank (standard deviation) LOQ = blank (mean) + 10× blank (standard deviation) blank), which was used to calculate the linear relationship.[27]

Results and discussion

Characterization of dye doped nanoparticles

First, we generated all materials and characterized them meticulously. FITC and RITC dye were used to form fluorescent silica nanoparticles ranging from 100 nm, 50 nm, and 25 nm as described.[26,28] TEM images (Fig. 2) unequivocally confirmed the uniformity of nanoparticle size, which was further quantified using ImageJ to generate size distribution histograms (Fig. 3), demonstrating the expected frequency of the target diameters. The particles surface of the nanoparticles was then modified with a polyethylene glycol spacer terminated with a carboxylic group to reduce nonspecific binding. Next, TCO or TZ was conjugated to the fluorescent silica nanoparticles by first activating the surface with EDC/NHS, followed by the addition of NH$_2$-PEG-TCO or NH$_2$-PEG-TZ. This process resulted in the formation of FITC-SiO$_2$-PEG$_{5k}$-TCO or FITC-SiO$_2$-PEG$_{5k}$-TZ, respectively.

Zeta potential measurements were used throughout the surface modification process of the fluorescent silica nanoparticles to confirm the success of each modification step and assess surface charge, a technique commonly applied in related studies such as fluorescence immunoassays on paper and bio responsive quantum dot-enzyme platforms.[29,30] Different surface chemistries exhibit varying surface potential charges, with the zeta potential of the dye-doped SiO$_2$-OH particles initially ranging from −25 mV to −9 mV, attributed to the presence of hydroxyl groups on the surface, as shown in Fig. 4. Upon coating the surface with amine functional groups, the zeta potential shifted to a positive range of +9 to +15 mV, clearly indicating the successful addition of the amine group. Next, bis-carboxylic PEG linker was conjugated to the surface, where the zeta potential ranged from −9 to −3 mV. Finally, the addition of TZ or TCO functionalities caused a dip in the zeta potential rendering it slightly negative which reflects the final modification.

Functional and photostability

We evaluated the performance of each dye doped fluorescent silica nanoparticles at the same weight concentration. Next the excitation and emission spectra of equivalent weighted particles was measured and compared (Fig. S1 and S2†) for RITC and FITC. The results showed that nanoparticles with a size of 100 nm exhibited the
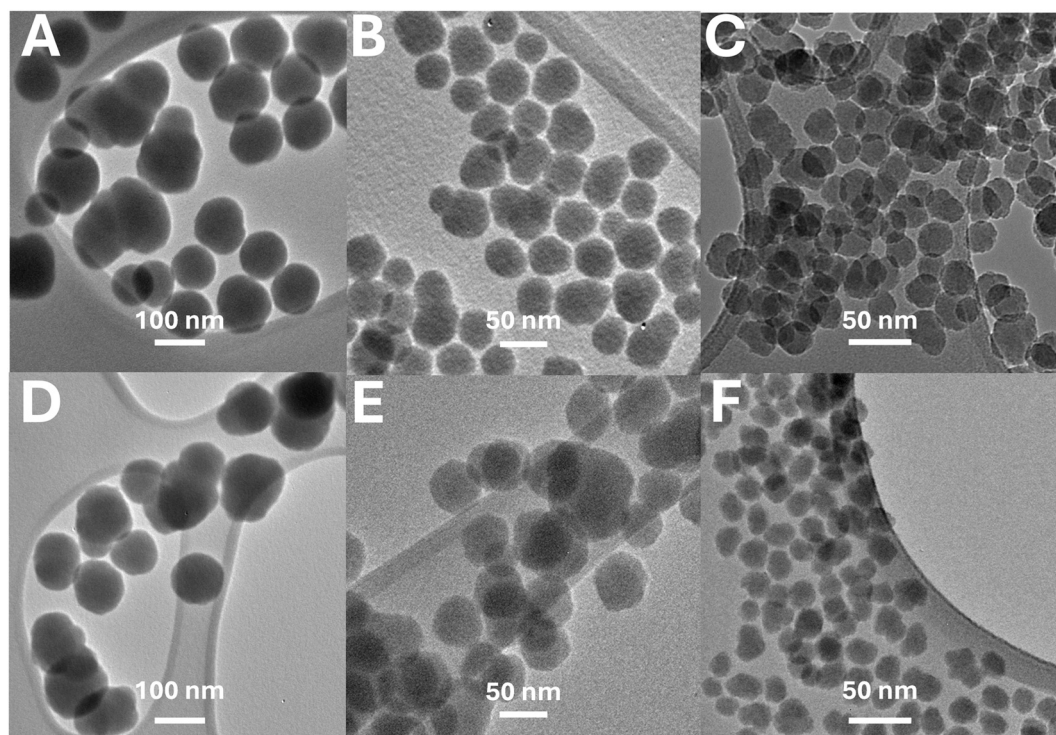

Fig. 2   TEM images of (A) 100 nm FITC-SiO$_2$-OH, (B) 50 nm FITC-SiO$_2$-OH, (C) 25 nm FITC-SiO$_2$-OH, (D) 100 nm RITC-SiO$_2$-OH, (E) 50 nm RITC-SiO$_2$-OH, (F) 25 nm RITC-SiO$_2$-OH.
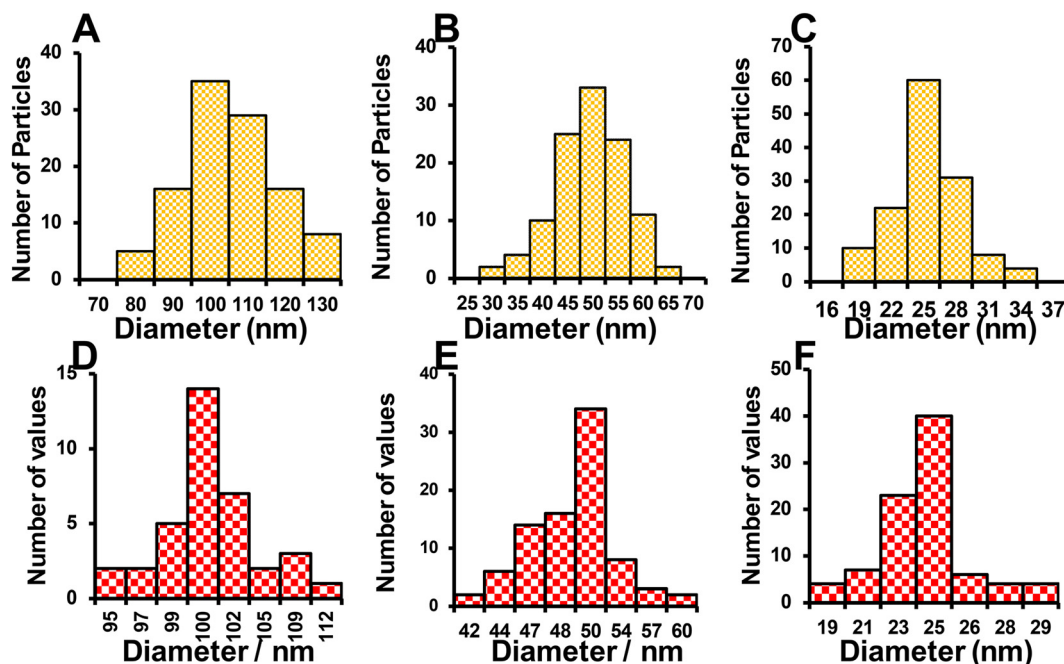
Fig. 3 Size distribution of (A) 100 nm FITC-SiO$_2$-OH, (B) 50 nm FITC-SiO$_2$-OH, (C) 25 nm FITC-SiO$_2$-OH, (D) 100 nm RITC-SiO$_2$-OH, (E) 50 nm RITC-SiO$_2$-OH, (F) 25 nm RITC-SiO$_2$-OH.
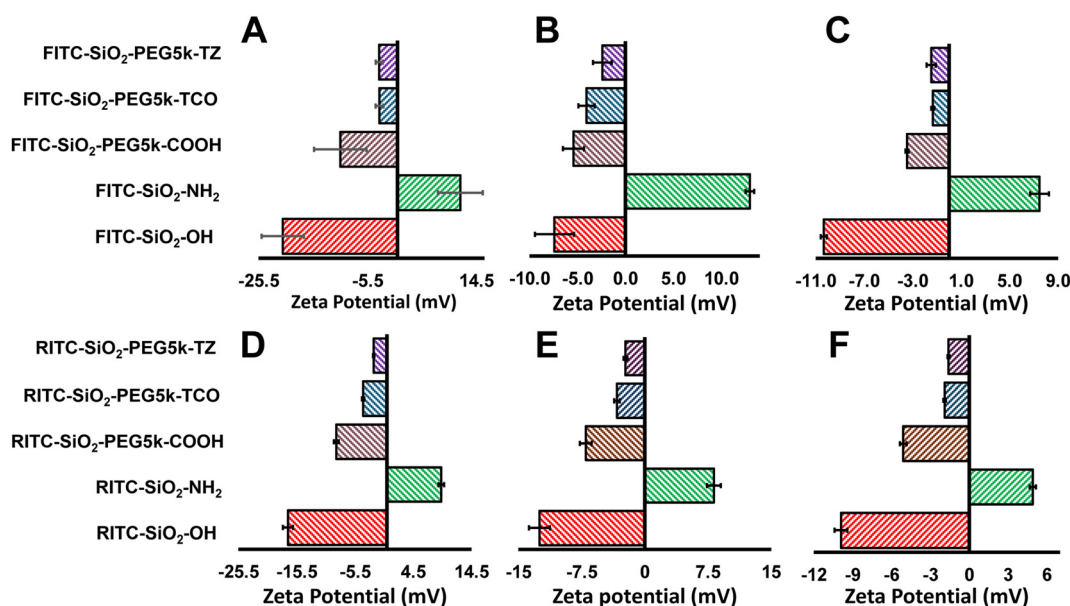

Fig. 4 Zeta potentials of fluorescent silica nanoparticles (A) FITC-SiO$_2$-R 100 nm, (B) FITC-SiO$_2$-R 50 nm, (C) FITC-SiO$_2$-R 25 nm, (D) RITC-SiO$_2$-R 100 nm, (E) RITC-SiO$_2$-R 50 nm, (F) RITC-SiO$_2$-R 25 nm. Error bars indicate the standard deviation of three measurements.

highest intensity, where 25 nm particles were the lowest intensity, all things being equal (Fig. S3†).

To ensure robustness we measured photostability and the functional stability of the TCO/TZ modified particles. Photostability studies show the particle fluorescence intensity remains stable over a month (Fig. S2†). Functional stability studies were conducted to assess the stability of TCO- and TZ-functionalized particles. Three concentrations of p24 antigen—control, 100 fg mL^{-1}, and 1 ng mL^{-1} were analyzed

weekly to determine any changes in performance trends. While a nonspecific binding increase was observed over the experiment, the overall trend in detection remained for three weeks (Fig. S3†).

Concentration optimization studies

To evaluate the optimal concentration of 50 nm fluorescent-doped nanoparticles for assay sensitivity, we tested three

concentrations: 25 μg, 50 μg, and 75 μg of FITC-SiO$_2$-TZ/TCO particles. At 25 μg (Fig. 4A), the assay achieved a limit of detection (LOD) of 150 fg mL^{-1} and a limit of quantification (LOQ) of 4 pg mL^{-1}, with a linear range of 150 fg mL^{-1} to 1 ng mL^{-1}. This concentration resulted in low non-specific binding and reduced variability but exhibited weaker signal intensity due to the limited number of particles. Increasing the concentration to 50 μg of particles (Fig. 4B) enhanced the LOD to 66 fg mL^{-1} and the LOQ to 1 pg mL^{-1}, with a linear range of 66 fg mL^{-1} to 1 ng mL^{-1}. This concentration provided an optimal balance between signal strength and non-specific binding, despite moderate levels of the latter. Further increasing the concentration to 75 μg (Fig. 4C) resulted in an excess of particles, raising the LOD significantly to 500 pg mL^{-1} and diminishing assay sensitivity. Therefore, 50 μg was identified as the optimal concentration, offering the best trade-off between signal strength and non-specific binding.

Packing optimization studies

We hypothesized that smaller nanoparticles would improve packing efficiency, as illustrated in Fig. 5. To estimate packing density, we calculated the binding capacity of a 96-well plate (Table 1), assuming 400–500 ng of IgG antibody can bind per cm^2 of the plate's surface area. For a 24 kDa p24 antibody (Ab$_1$), this corresponds to approximately 1.0×10^{13} to 1.25×10^{13} antibodies per cm^2, or 3.2×10^{12} antibodies per well, based on a binding density of 400 ng cm^{-2}. The concentration range

of p24 antigen in each well (200 μL) spans from 0.1 fg mL^{-1} to 10 μg mL^{-1}, translating to approximately 5.0×10^2 to 5.0×10^{16} antigens per well.

Using TEM analysis, we estimated approximately 6.7×10^7 dye-doped 50 nm particles per 1 μg. With an estimated particle binding area of 5.67×10^{-10} cm^2 and a total well surface area of 0.32 cm^2, the maximum particle binding capacity in a single layer was calculated to be 2.22×10^9 particles, equivalent to 33 μg of particles. These calculations underscore the importance of selecting appropriately sized nanoparticles and their concentrations to maximize assay sensitivity and minimize non-specific interactions. Layer-by-layer attachment of the particles are shown in confocal images (Fig. S5†). Increasing brightness of the particles are clearly visible in 2nd and 3rd layer.

Size comparison studies

Size comparison studies were performed, as shown in Fig. 6, with the hypothesis that smaller particles would yield a lower limit of detection (LOD) due to improved packing of the layers. Starting with 100 nm FITC-doped particles (Fig. 7A), we reduced the particle size to 50 nm (Fig. 7B), and finally to 25 nm (Fig. 7C). The LOD decreased from 163 fg mL^{-1} for the 100 nm particles to 66 fg mL^{-1} for the 50 nm particles, and further to 13 fg mL^{-1} for the 25 nm particles.

Similarly, the RITC-doped particles (Fig. 7D–F) exhibited a comparable trend, where particle size inversely affected the LOD. The 100 nm RITC-doped particles showed an initial LOD of 50 fg mL^{-1}, which decreased to 42 fg mL^{-1}
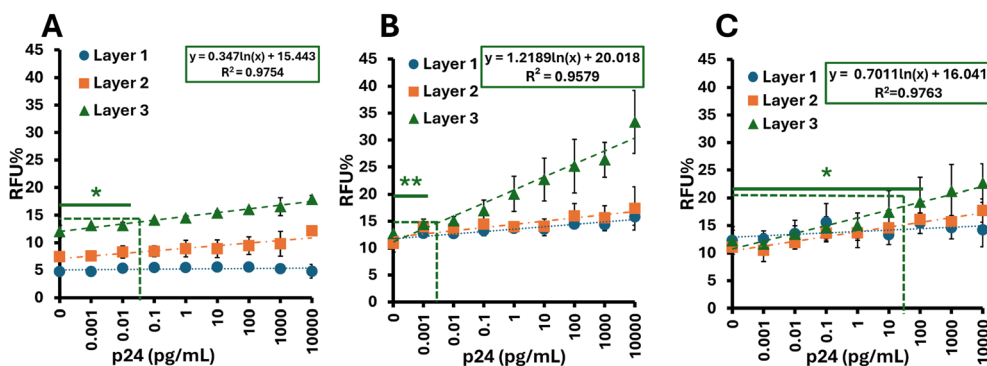

Fig. 5 Studies of different weight concentrations of 50 nm particles the signal value and different concentrations of p24 antigen, concentration optimization for 50 nm FITC-SiO$_2$-TCO/TZ (A) 25μg (B) 50 μg (C) 75 μg. The y-axis, % RFU, is the percent relative fluorescence intensity of the sample as a function of an internal control. Error bars indicate the standard deviations of three measurements (ns > 0.05, *p < 0.05.)

Table 1 Quantification of nanoparticles

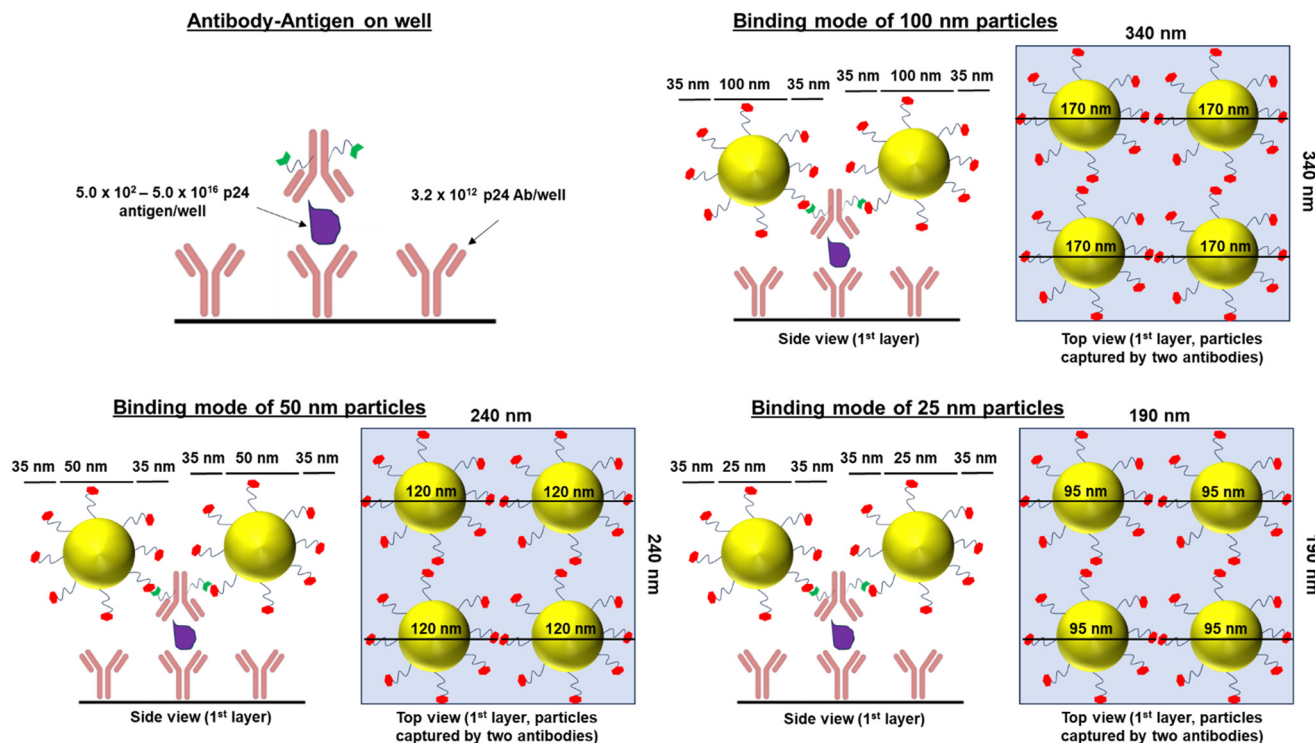| Entry	100 nm	50 nm	25 nm
Area covered by 4 particles (A1)	1.156×10^{-9} cm^2	5.76×10^{-10} cm^2	3.61×10^{-10} cm^2
Surface area of well (A2)	0.32 cm^2	0.32 cm^2	0.32 cm^2
Average length of PEG$_{5k}$	35 nm	35 nm	35 nm
Max NPs fit in 1st layer {N1 = 4(A2/A1)}	1.10×10^9	2.22×10^9	3.55×10^9
No of NPs in 1 μg (N2)	1.5×10^7	6.7×10^7	1.65×10^8
NPs required (μg) to cover the well surface (N1/N2)	73 μg	33 μg	21 μg

Fig. 6 Theoretical packing density calculation of different sized (100 nm, 50 nm, and 25 nm) nanoparticles and number of antigen and antibody per well of 96 well plate during the assay.
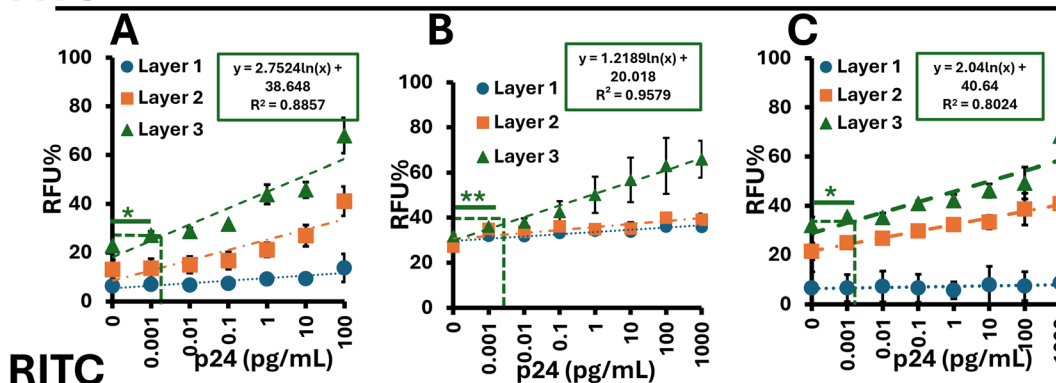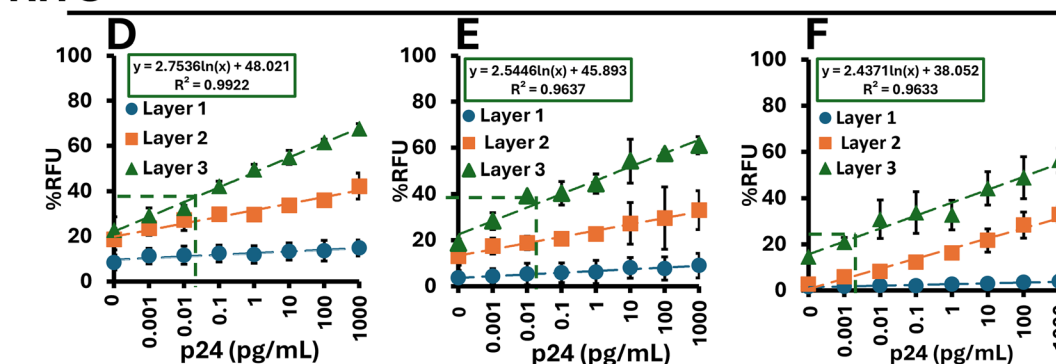

Fig. 7 Signal response of the sandwich immunoassay using multiple layers. (A) FITC 100 nm, (B) FITC 50 nm, (C) FITC 25 nm, (D) RITC 100 nm, (E) RITC 50 nm, (F) RITC 25 nm. The y-axis, % RFU, is the percent of relative fluorescence intensity of the sample as a function of an internal control. Error bars indicate the standard deviation of three measurements performed on three separate days.

© 2025 The Author(s). Published by the Royal Society of Chemistry

Table 2 Summary of assay results

Nanoparticle type	LOD (fg ml^{-1})	Linear range	Linearity (R^2)
100 nm FITC	163	0.163–1 ng mL^{-1}	0.86
50 nm FITC	66	0.0066–1 ng mL^{-1}	0.98
25 nm FITC	13	0.0013–1 ng mL^{-1}	0.81
100 nm RITC	50	0.0504–1 ng mL^{-1}	0.99
50 nm RITC	42	0.0420–1 ng mL^{-1}	0.96
25 nm RITC	7	0.0072–1 ng mL^{-1}	0.94

with the 50 nm particles, and 7 fg mL^{-1} with the 25 nm particles. These results, along with the extended linear range, are summarized in Table 2. Notably, the linear range extended from 7 fg mL^{-1} to 1 ng mL^{-1} with the 25 nm RITC-doped particles.

Dye comparison studies

When comparing dyes to dyes regardless of particle size we see that RITC-doped particles vastly outperform their FITC counterparts, this is likely due to the increase "brightness" of the fluorophore. We see this trend repeated in 100 nm FITC and 100 nm doped RITC particles in Fig. 7A and D respectively, 50 nm FITC and 50 nm doped RITC particles in Fig. 7B and E respectively, and for the 25 doped particles in Fig. 7C and F.

Comparison with standard ELISA

To benchmark the performance of our novel assay, we conducted a direct comparison with a commercially available ELISA kit (human, mouse, & rat HIV-1 Gag p24 ELISA Kit – Quantikine, R&D Systems), which was enhanced with Amplex™ Red and Amplex™ UltraRed fluorescent substrates to align with the fluorescence-based nature of our method. The commercial ELISA demonstrated a linear range of 7.8–500 pg mL^{-1} and a limit of detection (LOD) of 3.35 pg mL^{-1} as seen in Fig. 8A. In contrast, our layer-by-layer

amplification assay, incorporating 25 nm RITC-doped nanoparticles, exhibited a markedly superior performance with an LOD of 7 fg mL^{-1} and an extended linear range of 0.0072–1 ng mL^{-1} in layer 3 (Fig. 8B). Our assay offers over eight orders of magnitude greater sensitivity and a broader dynamic range than the commercial ELISA. Furthermore, as shown in Table 3, a direct comparison of our assay with other bioanalytical sensors for p24 demonstrates that our platform achieves superior sensitivity and an unmatched linear range.

Conclusions

We successfully synthesized and characterized FITC- and RITC-doped silica nanoparticles ranging in size from 25 nm, 50 nm, and 100 nm. Particle sizes were confirmed *via* TEM, while ImageJ analyses and zeta potential measurements validated surface modifications, including the addition of polyethylene glycol spacers and TCO or TZ functionalities. These nanoparticles were employed in an extensive comparative study to enhance the ultrasensitive detection of the HIV-1 p24 antigen. By leveraging bioorthogonal chemistries and advanced signal amplification techniques, we optimized their detection capabilities for improved sensitivity in point-of-care applications. Our bioorthogonal layer-by-layer approach differs from conventional multivalent binding (*e.g.*, streptavidin–biotin) by reducing steric hindrance and enhancing binding kinetics, improving target accessibility and signal amplification. This is because we are using two small molecules that are much smaller in size compared to avidin, which is a protein. The advancement of multifunctional nanoparticles in diagnostics can significantly benefit from the use of mutually orthogonal combinations.[38]

RITC-doped nanoparticles consistently outperformed FITC-doped counterparts, offering superior signal enhancement, due to improved molecular brightness. Our findings further validated that smaller nanoparticles enhance packing density, significantly lowering the limits of detection
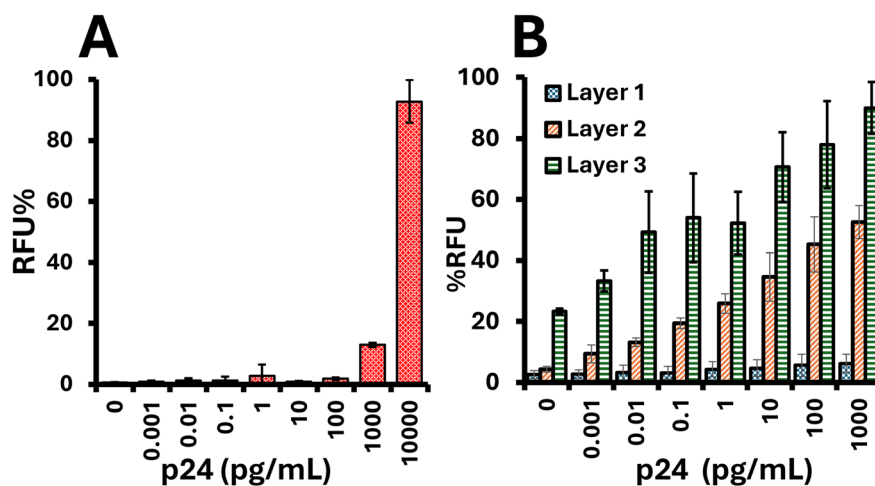

Fig. 8 Comparison of detection sensitivity: (A) commercially available ELISA for HIV p24 antigen detection and (B) enhanced layer-by-layer amplification assay using 25 nm RITC-doped nanoparticles, highlighting the improved sensitivity and linear range of our method.

Table 3 Comparison of analytical sensitivity to other p24 biosensors

Detection methods	Strategy	LOD	Detection range	Reference	Year
Fluorescence	Streptavidin-conjugated AuNCs	5.0 pg mL^{-1}	Up to 1000 pg mL^{-1}	31	2018
Fluorescence and visual	TdT, CuNPs	0.025 fg mL^{-1}	0.025–1000 fg mL^{-1}	32	2022
LFIA-naked eye	PtNCs, CN/DAB	0.8 pg mL^{-1}	0.8–10 000 pg mL^{-1}	33	2018
Fluorescence	Streptavidin labeled FSN	8.2 pg mL^{-1}	8.2–1000 pg mL^{-1}	34	2017
Fluorescence	β-Sheets bind with Congo red	0.61 pg mL^{-1} (3F-based)	0.61–150 pg mL^{-1}	35	2020
		2.44 pg mL^{-1} (2F-based)	2.44–150 pg mL^{-1}		
PEC	ALP-encapsulated liposomes	0.63 pg mL^{-1}	0.63–50 000 pg mL^{-1}	36	2018
Electrochemical	Fe$_3$O$_4$@SiO$_2$Ab$_1$/AuNPs/EV-p24 Ab$_2$	0.5 pg mL^{-1}	0.5–10 000 pg mL^{-1}	37	2013
Fluorescence	Layer-by-layer signal amplification	0.017 pg mL^{-1} (PBS)	0.017–10 000 pg mL^{-1}	17	2024
		0.046 pg mL^{-1} (serum)	0.046–10 000 pg mL^{-1}		
Fluorescence	**Layer-by-layer signal amplification**	**0.007 pg mL^{-1}**	**0.007–10 000 pg mL^{-1}**	**This work**	**2024**

(LOD). Notably, the 3rd layer of 25 nm RITC-doped nanoparticles demonstrated a LOD of 7 fg mL^{-1} and an extended linear range from 7 fg mL^{-1} to 1 ng mL^{-1}. — eliminating the need for sample dilution, even with highly concentrated specimens. This broad linear range spanning seven orders of magnitude simplifies sample preparation, reduces the risk of dilution errors, and makes the assay more user-friendly and efficient. Beyond HIV-1 p24 antigen detection, these developments demonstrate the platform's potential for diverse diagnostic applications requiring sensitive detection of low analyte concentrations. The method offers a broad linear range that eliminates the need for sample dilution when detecting multiple biomarkers. However, challenges remain, including limited nanoparticle stability (3 weeks at rt and the requirement of multiple wash steps) which can increase assay complexity and time. We are actively working to improve nanoparticle stability and streamline the process for point-of-care diagnostics.

Data availability

The data supporting this article have been included as part of the ESI.†

Conflicts of interest

There are no conflicts to declare.

Acknowledgements

References

1 UNAIDS, *Global HIV & AIDS statistics — Fact sheet*, 2024.

2 S. Payagala and A. Pozniak, *Clin. Dermatol.*, 2024, **42**, 119–127.

3 M. Wu, B. Yang, L. Shi, Q. Tang, J. Wang, W. Liu, B. Li and Y. Jin, *Anal. Chim. Acta*, 2024, **1304**, 342553.

4 E. M. Girardi, C. A. P. Sabin, A. d'Arminio and M. Monforte, *JAIDS, J. Acquired Immune Defic. Syndr.*, 2007, **46**, S3.

5 G. Pantaleo, B. Correia, C. Fenwick, V. S. Joo and L. Perez, *Nat. Rev. Drug Discovery*, 2022, **21**, 676–696.

6 P. Patel, D. Mackellar, P. Simmons, A. Uniyal, K. Gallagher, B. Bennett, T. J. Sullivan, A. Kowalski, M. M. Parker, M. LaLota, P. Kerndt, P. S. Sullivan and Centers for Disease Control and Prevention Acute HIV Infection Study Group, *Arch. Intern. Med.*, 2010, **170**, 66–74.

7 S. Tian, L. Huang, Y. Gao, Z. Yu and D. Tang, *Sens. Diagn.*, 2023, **2**, 707–713.

8 N. Uno, Z. Li, L. Avery, M. M. Sfeir and C. Liu, *Anal. Chim. Acta*, 2023, **1262**, 341258.

9 T. Liu, A. J. Politza, A. Kshirsagar, Y. Zhu and W. Guan, *ACS Sens.*, 2023, **8**, 4716–4727.

10 L. Abuogi, L. Noble and C. Smith, *Pediatrics*, 2024, **153**, e2024066843.

11 K. A. Veldsman, B. Laughton, A. Janse van Rensburg, P. Zuidewind, E. Dobbels, S. Barnabas, S. Fry, M. F. Cotton and G. U. van Zyl, *AIDS*, 2021, **35**, 1247.

12 M. M. Bond and R. R. Richards-Kortum, *Am. J. Clin. Pathol.*, 2015, **144**, 885–894.

13 E. Cheah, D. P. Tran, M. T. Amen, R. D. Arrua, E. F. Hilder and B. Thierry, *Anal. Chem.*, 2022, **94**, 1256–1263.

14 S. Tang, J. Zhao, A. Wang, R. Viswanath, H. Harma, R. F. Little, R. Yarchoan, S. L. Stramer, P. N. Nyambi, S. Lee, O. Wood, E. Y. Wong, X. Wang and I. K. Hewlett, *Clin. Vaccine Immunol.*, 2010, **17**, 1244–1251.

15 N. E. Rosenberg, C. D. Pilcher, M. P. Busch and M. S. Cohen, *Curr. Opin. HIV AIDS*, 2015, **10**, 61.

16 E. R. Gray, R. Bain, O. Varsaneux, R. W. Peeling, M. M. Stevens and R. A. McKendry, *AIDS*, 2018, **32**, 2089–2102.

17 T. Jia, V. Saikam, Y. Luo, X. Sheng, J. Fang, M. Kumar and S. S. Iyer, *ACS Omega*, 2024, **9**, 14604–14612.

18 K. Wang, X. He, X. Yang and H. Shi, *Acc. Chem. Res.*, 2013, **46**, 1367–1376.

19 C. Xie, D. Yin, J. Li, L. Zhang, B. Liu and M. Wu, *Nano Biomed. Eng.*, 2009, **1**, 27–31.

20 A. H. Ashoka, I. O. Aparin, A. Reisch and A. S. Klymchenko, *Chem. Soc. Rev.*, 2023, **52**, 4525–4548.

21 L. D. Lavis and R. T. Raines, *ACS Chem. Biol.*, 2008, **3**, 142–155.

22 J. B. Grimm and L. D. Lavis, *Nat. Methods*, 2022, **19**, 149–158.

23 J. B. Grimm, B. P. English, J. Chen, J. P. Slaughter, Z. Zhang, A. Revyakin, R. Patel, J. J. Macklin, D. Normanno and R. H. Singer, *Nat. Methods*, 2015, **12**, 244–250.

24 I. McKay, D. Forman and R. White, *Immunology*, 1981, **43**, 591.

25 H. N. Kim, M. H. Lee, H. J. Kim, J. S. Kim and J. Yoon, *Chem. Soc. Rev.*, 2008, **37**, 1465–1472.

26 M. L. Vera, A. Cánneva, C. Huck-Iriart, F. G. Requejo, M. C. Gonzalez, M. L. Dell'Arciprete and A. Calvo, *J. Colloid Interface Sci.*, 2017, **496**, 456–464.

27 S.-W. Lin, C.-F. Shen, C.-C. Liu and C.-M. Cheng, *Front. Bioeng. Biotechnol.*, 2021, **9**, 752681.

28 G. Durgun, K. Ocakoglu and S. Ozcelik, *J. Phys. Chem. C*, 2011, **115**, 16322–16332.

29 S. Lv, Y. Tang, K. Zhang and D. Tang, *Anal. Chem.*, 2018, **90**, 14121–14125.

30 Z. Qiu, J. Shu and D. Tang, *Anal. Chem.*, 2017, **89**, 5152–5160.

31 A. D. Kurdekar, L. A. Avinash Chunduri, C. S. Manohar, M. K. Haleyurgirisetty, I. K. Hewlett and K. Venkataramaniah, *Sci. Adv.*, 2018, **4**, eaar6280.

32 P. Chen, Z. Tang, K. Huang, Y. Wei, D. Li, Y. He, M. Li, D. Tang, Y. Bai, Y. Xie, J. Huang, C. Tao and B. Ying, *Sens. Actuators, B*, 2022, **354**, 131209.

33 C. N. Loynachan, M. R. Thomas, E. R. Gray, D. A. Richards, J. Kim, B. S. Miller, J. C. Brookes, S. Agarwal, V. Chudasama, R. A. McKendry and M. M. Stevens, *ACS Nano*, 2018, **12**, 279–288.

34 A. D. Kurdekar, L. A. A. Chunduri, S. M. Chelli, M. K. Haleyurgirisetty, E. P. Bulagonda, J. Zheng, I. K. Hewlett and V. Kamisetti, *RSC Adv.*, 2017, **7**, 19863–19877.

35 H. Cao, Y. Liu, H. Sun, Z. Li, Y. Gao, X. Deng, Y. Shao, Y. Cong and X. Jiang, *Anal. Chem.*, 2020, **92**, 11089–11094.

36 J. Zhuang, B. Han, W. Liu, J. Zhou, K. Liu, D. Yang and D. Tang, *Biosens. Bioelectron.*, 2018, **99**, 230–236.

37 N. Gan, X. Du, Y. Cao, F. Hu, T. Li and Q. Jiang, *Materials*, 2013, **6**, 1255–1269.

38 W. R. Algar, D. E. Prasuhn, M. H. Stewart, T. L. Jennings, J. B. Blanco-Canosa, P. E. Dawson and I. L. Medintz, *Bioconjugate Chem.*, 2011, **22**, 825–858.